Inorg. Chem. **2007**, *46*, 4167−4176

Crystal Structures and in-Situ Formation Study of Mayenite Electrides

Luis Palacios,[†] Ángeles G. De La Torre,[†] Sebastián Bruque,[†] Jose L. García-Muñoz,[‡] Santiago García-Granda,[§] Denis Sheptyakov,[||] and Miguel A. G. Aranda*,[†]

Dept. Química Inorgánica, Universidad de Málaga, Campus Teatinos, 29071-Málaga, Spain, Institut de Ciència de Materials de Barcelona, CSIC, Campus Universitari de Bellaterra, E-08193 Bellaterra, Spain, Dept. de Química Física y Analítica, Universidad de Oviedo, C/Julián Clavería, 33006-Oviedo, Spain, and Laboratory for Neutron Scattering, ETH Zurich & PSI Villigen, CH-5232 Villigen PSI, Switzerland

Received January 11, 2007

Mayenite inorganic electrides are antizeolite nanoporous materials with variable electron concentration $[Ca_{12}Al_{14}O_{32}]^{2+}\square_{5-\delta}O_{1-\delta}{}^{2-}e_{2\delta}{}^{-}$ ($0 < \delta \leq 1$), where $\square$ stands for empty sites. The oxymayenite crystal structure contains positively charged cages where loosely bounded oxide anions are located. These oxygens can be removed to yield electron-loaded materials in which the electrons behave like anions (electrides). Here, a new preparation method, which allows synthesizing powder mayenite electrides easily, is reported. Accurate structural data for the white ($\delta = 0$) and green electride ($\delta \sim 0.5$) are reported from joint Rietveld refinements of neutron and synchrotron X-ray powder diffraction data and also from single-crystal diffraction. The electride formation at high temperature under vacuum has been followed in-situ by neutron powder diffraction. The evolution of mayenite crystal structure, including the changes in the key occupation factor of the intracage oxide anions, is reported. Furthermore, the stability of mayenite framework in very low oxygen partial pressure conditions is also studied. It has been found that C12A7 decomposes, at 1373 K in reducing conditions, to give $Ca_5Al_6O_{14}$ (C5A3) and $Ca_3Al_2O_6$ (C3A). The kinetics of this transformation has also been studied. The fit of the transformed fraction to the classic Avrami–Erofe'ev equation gave an "Avrami exponent", $n = 2$, which indicates that nucleation is fast and the two-dimensional linear growth of the new phases is likely to be the limiting factor.

Introduction

Electrides are a family of materials which are attracting increasing attention because of their possible technological applications such as catalysts, low-temperature electron emitters, or thermoionics.[1,2] They have been defined as ionic compounds in which electrons are located in a crystallographic site, not belonging to a particular atom, and behaving like anions.[3] Organic electrides did not have thermal and chemical stability at room temperature (RT),[4−6] which has impeded their applications, with the exception of a recently developed compound.[7] Some of these problems can be overcome by synthesizing RT stable electrides derived from mayenite, $12CaO{\cdot}7Al_2O_3$ (C12A7).[8] Practical applications,[9−12] including some derived from the coexistence of transparency and electrical conductivity, could be more

* To whom correspondence should be addressed. E-mail: g_aranda@uma.es.
[†] Universidad de Málaga.
[‡] Campus Universitari de Bellaterra.
[§] Universidad de Oviedo.
[||] ETH Zurich & PSI Villigen.

(1) Huang, R. H.; Dye, J. L. *Chem. Phys. Lett.* **1990**, *166*, 133−136.
(2) Petkov, V.; Billinge, S. J. L.; Vogt, T.; Ichimura, A. S.; Dye, J. L. *Phys. Rev. Lett.* **2002**, *89*, 75502.
(3) Dye, J. L. *Science* **2003**, *301*, 607−608.
(4) Huang, R. H.; Faber, M. K.; Moeggenborg, K. J.; Ward, D. L.; Dye, J. L. *Nature* **1988**, *331*, 599−601.
(5) Wagner, M. J.; Huang, R. H.; Eglin, J. L.; Dye, J. L. *Nature* **1994**, *368*, 726−729.
(6) Dawes, S. B.; Eglin, J. L.; Moeggenborg, K. J.; Kim, J. N.; Dye, J. L. *J. Am. Chem Soc.* **1991**, *113*, 1605−1609.
(7) Redko, M. Y.; Jackson, J. E.; Huang, R. H.; Dye, J. L. *J. Am. Chem. Soc.* **2005**, *127*, 12416−12422.
(8) Matsuishi, S.; Toda, Y.; Miyakawa, M.; Hayashi, K.; Kamiya, T.; Hirano, M.; Tanaka, I.; Hosono, H. *Science* **2003**, *301*, 626−629.
(9) Toda, Y.; Matsuishi, S.; Hayashi, K.; Ueda, K.; Kamiya, T.; Hirano, M.; Hosono, H. *Adv. Mater.* **2004**, *16*, 685−689.
(10) Kamiya, T.; Aiba, S.; Miyakawa, M.; Nomura, K.; Matsuishi, S.; Hayashi, K.; Ueda, K.; Hirano, M.; Hosono, H. *Chem. Mater.* **2005**, *17*, 6311−6316.
(11) Kamioka, H.; Hiramatsu, H.; Hayashi, K.; Hirano, M.; Hosono, H. *J. Photochem. Photobiol., A* **2004**, *166*, 141−147.
(12) Hosono, H. *Sci. Technol. Adv. Mater.* **2004**, *5*, 409−416.

10.1021/ic0700497 CCC: $37.00
Published on Web 04/14/2007

easily developed due to the stability of these materials. These applications may include components for flat displays or solar cells.

C12A7 is known as a major phase of high alumina cements, and it has a body-centered cubic structure, $I\bar{4}3d$ space group, with a lattice constant of 11.99 Å and a unit cell chemical content of $Ca_{24}Al_{28}O_{66}$. Its crystal structure was first determined from single-crystal data,[13] and it was later revisited by neutron powder diffraction data.[14] The structure of C12A7 can be described as an antizeolite-type framework with positively charged cages that can accommodate a variety of anionic species such as halides,[15] O_2^-,[16] O_2^{2-},[17] O^-,[18] OH^-,[15] H^-,[19] and even electrons.[8] Due to its nanoporous framework, the structural formula can be expressed as $[Ca_{12}Al_{14}O_{32}]^{2+}\square_5O^{2-}$, representing one oxide anion randomly distributed over six cages (per formula unit). The presence of empty cages allows water and oxygen uptake at high temperature[20−22] and even oxide conductivity.[23,24]

Electron-loaded mayenite constitutes a series $[Ca_{12}Al_{14}O_{32}]^{2+}\square_{5-\delta}O_{1-\delta}{}^{2-}e_{2\delta}{}^-$ ($0 \le \delta \le 1$) ranging from $\delta = 0$ in the white insulating oxymayenite, $[Ca_{12}Al_{14}O_{32}]^{2+}\square_5O^{2-}$, to $\delta = 1$ in the black conducting compound, $[Ca_{12}Al_{14}O_{32}]^{2+}\square_4e_2{}^-$, being green for intermediate electron concentrations. So far four methods have been reported to prepare these electron-loaded main elements oxides: (i) calcium vapor treatment under low pressures,[8] which requires mayenite single crystals[25] and long annealing times (over 10 days), which is unsuitable for efficiently fabricating large amounts of electride samples; (ii) treatment with hydrogen gas at high temperature followed by UV-light illumination, which produces the photodissociation of the occluded hydride anions and the release of electrons into the cages;[19,26] (iii) direct solidification of a graphite-reduced C12A7 melt[27,28] followed by crystallization of the transparent glass (glass-ceramics process); (iv) treating C12A7 powders at high-temperature (1000−1200 °C) under N_2 flow using a carbon crucible with cap to generate a CO/CO_2 rich atmosphere inside the crucible.[29]

Several theoretical studies dedicated to mayenite electrides have been reported resulting in different and often contradictory descriptions. The first work[30] supported the electride model with localized extra electrons, whereas a subsequent study[31] concluded that the extra electrons were highly delocalized both inside the cavities and in the regions occupied by cations, thus being in contradiction with the electride model. A subsequent work, which used topological analysis of electron-localization functions to classify chemical bonds, gave a model with electrons partially localized into the cages.[32] Hence, the degree of localization of electrons in a single cage remains an open issue that deserves experimental and further theoretical studies. Furthermore, the electron delocalization degree may change with the electron density along the mayenite series, $[Ca_{12}Al_{14}O_{32}]^{2+}\square_{5-\delta}O_{1-\delta}{}^{2-}e_{2\delta}{}^-$ ($0 \le \delta \le 1$). Experimental results of transport properties, and theoretical calculations, suggest a change from highly localized (electrons behaving like anions, electride model) for low electron loadings to highly delocalized for very large electron loadings.[8,30−34] Therefore, the proper identification of C12A7 electron-doped samples as electrides probably depends on the electron loading. Moreover, there have been some studies dedicated to the photodissociation of the hydrogen-containing mayenite, which yields a persistent transparent conducting electron-loaded mayenite.[35−37] Band structure and properties of these materials (H-doped/UV-irradiated mayenites) may be quite different from that of mayenite electrides, where the extraframework oxygens are removed.[33]

Here, we report a new route for the preparation of electron-loaded mayenites using vanadium foils as deoxygenating agent. We also give accurate structural descriptions of stoichiometric and electron-loaded derivatives by using Rietveld analyses of joint neutron and X-ray synchrotron powder diffraction data. The formation of mayenite electride at high temperature under vacuum in a vanadium container was followed in-situ by neutron powder diffraction. The decomposition kinetics of the electride at 1373 K in reducing conditions has also been studied.

(13) Bartl, H.; Scheller, T. *Neues Jahrb. Mineral. Monatsh.* **1970**, *35*, 547−552.
(14) Christensen, A. N. *Acta Chem. Scand. A* **1987**, *41*, 110−112.
(15) Jeevaratnam, J.; Glasser, F. P.; Glasser, L. S. D. *J. Am. Ceram. Soc.* **1964**, *47*, 105−106.
(16) Hosono, H.; Abe, Y. *Inorg. Chem.* **1987**, *26*, 1192−1195.
(17) Hayashi, K.; Hirano, M.; Hosono, H. *Chem. Lett.* **2005**, *34*, 586−587.
(18) Hayashi, K.; Hirano, M.; Matsuishi, S.; Hosono, H. *J. Am. Chem. Soc.* **2002**, *124*, 738−739.
(19) Hayashi, K.; Matsuishi, S.; Kamiya, T.; Hirano, M.; Hosono, H. *Nature* **2002**, *419*, 462−465.
(20) Hayashi, K.; Hirano, M.; Hosono, H. *J. Phys. Chem. B* **2005**, *109*, 11900−11906.
(21) Hayashi, K.; Matsuishi, S.; Hirano, M.; Hosono, H. *J. Phys. Chem. B* **2004**, *108*, 8920−8925.
(22) Hayashi, K.; Ueda, N.; Hirano, M.; Hosono, H. *Solid State Ionics* **2004**, *173*, 89−94.
(23) Lacerda, M.; Irvine, J. T. S.; Glasser, F. P.; West, A. R. *Nature* **1988**, *332*, 525−526.
(24) Irvine, J. T. S.; Lacerda, M.; West, A. R. *Mater. Res. Bull.* **1988**, *23*, 1033−1038.
(25) (a) Watauchi, S.; Tanaka, I.; Hayashi, K.; Hirano, M.; Hosono, H. *J. Cryst. Growth* **2002**, *237*, 801−805. (b) Kurashige, K.; Toda, Y.; Matstuishi, S.; Hayashi, K.; Hirano, M.; Hosono, H. *Cryst. Growth Des.* **2006**, *6*, 1602−1605.
(26) Hayashi, K.; Sushko, P. V.; Shluger, A. L.; Hirano, M.; Hosono, H. *J. Phys. Chem. B* **2005**, *109*, 23836−23842.
(27) Kim, S. W.; Miyakawa, M.; Hayashi, K.; Sakai, T.; Hirano, M.; Hosono, H. *J. Am. Chem. Soc.* **2005**, *127*, 1370−1371.
(28) Kim, S. W.; Toda, Y.; Hayashi, K.; Hirano, M.; Hosono, H. *Chem. Mater.* **2006**, *18*, 1938−1944.
(29) Kim, S. W.; Hayashi, K.; Hirano, M.; Hosono, H.; Tanaka, I. *J. Am. Ceram. Soc.* **2006**, *89*, 3294−3298.
(30) Sushko, P. V.; Shluger, A. L.; Hayashi, K.; Hirano, M.; Hosono, H. *Phys. Rev. Lett.* **2003**, *91*, 126401.
(31) Medvedeva, J. E.; Freeman, A. J.; Bertoni, M. I.; Mason, T. O. *Phys. Rev. Lett.* **2004**, *93*, 016408.
(32) Li, Z. Y.; Yang, J. L.; Hou, J. G.; Zhu, Q. S. *Angew. Chem., Int. Ed.* **2004**, *43*, 6479−6482.
(33) Medvedeva, J. E.; Freeman, A. J. *Appl. Phys. Lett.* **2004**, *85*, 955−957.
(34) Sushko, P. V.; Shluger, A. L.; Hayashi, K.; Hirano, M.; Hosono, H. *Mater. Sci. Eng., C* **2005**, *25*, 722−726.
(35) Sushko, P. V.; Shluger, A. L.; Hayashi, K.; Hirano, M.; Hosono, H. *Phys. Rev. B* **2006**, *73*, 014101.
(36) Medvedeva, J. E.; Freeman, A. J. *Europhys. Lett.* **2005**, *69*, 583−587.
(37) Sushko, P. V.; Shluger, A. L.; Hayashi, K.; Hirano, M.; Hosono, H. *Appl. Phys. Lett.* **2005**, *86*, 092101.

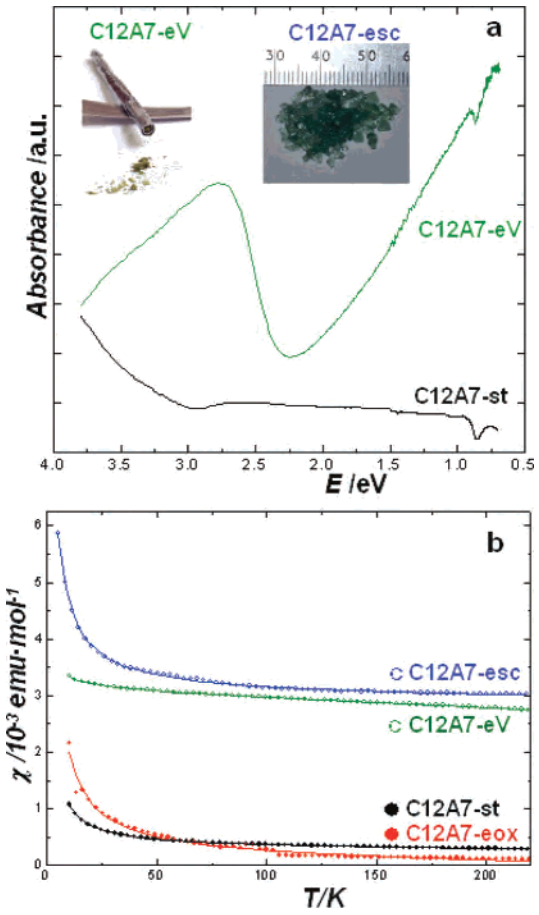

Figure 1. (a) Optical spectra for white C12A7-st (black line) and green C12A7-eV (green line). The top left inset shows a photograph of the as-synthesized C12A7-eV powder inside the vanadium rolled foil. The top right inset shows a photograph of the as-synthesized C12A7-esc crushed crystals. (b) Temperature dependence of the FC magnetic susceptibility for C12A7-st (black solid circles), C12A7-eV (green open circles), C12A7-esc (blue open circles), and C12A7-eox (red solid circles). The experimental points have been fitted to a sum of Pauli paramagnetic and Curie−Weiss contributions to the susceptibility. The temperature-independent χ_0 values are given in Table 1: C values range $(3-21) \times 10^{-3}$ emu·mol^{-1}·K; Θ values range from −0.3 to −2.0 K.

Experimental Section

Syntheses. Stoichiometric mayenite (hereafter labeled as C12A7-st) was synthesized by solid-state reaction between $CaCO_3$ (Alfa Chelometric standard) and γ-Al_2O_3 (Alfa 99.997%) at 1623 K for 16 h in air. The powders were quenched from 1373 K in a dry atmosphere to avoid the uptake of water and oxygen, which takes place between 773 and 1173 K.[21,38] A 3 g sample of C12A7-st was treated at 823 K in a tubular furnace under oxygen flow ($p(O_2) = 1$ bar) for 4 days, to obtain an oxygen-rich mayenite.[21] The resulting white sample (hereafter labeled as C12A7-O_2) was used in the HT-NPD study for in-situ generation of the electride, C12A7-e (see Powder Diffraction subsection). C12A7-st, ∼1 g, was also placed into a rolled vanadium foil and treated at 1273 K under vacuum (4×10^{-5} mbar) for 24 h in a silica glass tube. The resulting green powder (C12A7-eV; see a photograph in the inset of Figure 1a) has vanadium content slightly smaller than 60 ppm, determined by inductively coupled plasma. C12A7-eV was heated in air at 1473 K for 12 h and quenched regenerating a white powder (C12A7-eox). Green mayenite crystals were grown by direct solidification from a melt at 1723 K in a Pt 10% Rh ZGS crucible under ambient furnace atmosphere. The sample was cooled between 1723 and 1613 K, 0.1 K/min rate, and quenched. The green transparent solid was crashed into small pieces (C12A7-esc; see a photograph also in the inset of Figure 1a). Finally, C12A7-esc crystals were heated in air at 1623 K for 1 h and then quenched in the same way that C12A7-st, yielding colorless crystals (C12A7-osc).

Spectroscopy. Both stoichiometric, C12A7-st, and oxygen-loaded mayenite, C12A7-O_2, samples were initially characterized by Raman spectroscopy using a Fourier-transform Bruker Equinox 55 spectrometer. The Raman module used the 1055 nm excitation radiation supplied by a Nd:YAG Laser. The emitted radiation was collected at 90° by a Ge detector cooled with liquid N_2.

Diffuse reflectance spectra for compact powdered samples of C12A7-st and C12A7-eV were recorded on a Shimadzu UV-3100 UV−visible−near-infrared spectrometer in the 4−0.5 eV range using $BaSO_4$ as reference.

Magnetic Characterization. Magnetic susceptibility measurements were performed, over the temperature range 10−300 K, using a SQUID magnetometer (Quantum Design). The temperature dependence of the dc magnetization was measured on heating after a field-cooled (FC) process ($H = 1000$ Oe).

Powder Diffraction. Room-temperature NPD data for C12A7-st, C12A7-eV, and C12A7-O_2 samples, loaded in vanadium cans, were collected on HRPT diffractometer[39] of SINQ (Villigen, Switzerland) using a wavelength of 1.154 Å. These patterns had very good statistics (overall counting time ∼5 h), and the data range was 5−160° (2θ) with a step size of 0.05°. High-temperature neutron powder diffraction (HT-NPD) data were taken for C12A7-O_2 under high vacuum (10^{-5} mbar) with the sample loaded in a vanadium container (strongly hand-pressed). Powder data were collected each 100 K on heating at 10 K/min rate, between 373 and 1373 K. To follow the reaction at high temperature, 12 diffraction patterns were collected at 1373 K. The data range was 5−160° (2θ) with a step size of 0.05° and counting for ∼40 min/pattern. A room-temperature pattern with high statistics was also collected for the final product of the in-situ study, C12A7-e. Low-temperature NPD patterns for C12A7-st and C12A7-eV were also collected using a conventional He cryostat.

Ultrahigh synchrotron X-ray powder diffraction (SXRPD) data for C12A7-st and C12A7-eV samples, loaded in glass capillaries, were collected on ID31 diffractometer of ESRF, European Synchrotron Radiation Facility (Grenoble, France). A short wavelength, $\lambda = 0.620745$ Å, was selected with a double-crystal Si(111) monochromator and calibrated using Si NIST ($a = 5.43094$ Å). High-temperature patterns were obtained using a hot-air blower. The overall data acquisition time for each pattern was ∼40 min at room temperature and ∼15 min on heating. The data range was 3−54° (in 2θ) (11.86−0.68 Å) at RT (room temperature) and 3−46° (in 2θ) (11.86−0.79 Å) for the variable-temperature patterns. The data from the multianalyzer Si(111) stage coupled with the scintillation detectors were normalized and summed up to 0.002° step size with local software to produce the final raw data.

Room-temperature laboratory X-ray powder diffraction (RT-LXRPD) data were collected for C12A7-O_2 on a Siemens D5000 automated diffractometer using secondary graphite-monochromated Cu $K\alpha_{1,2}$ radiation. A RT-LXRPD pattern was collected for green C12A7-e on a PANalytical X'Pert Pro automated diffractometer, equipped with a Ge(111) primary monochromator (Cu $K\alpha_1$ radia-

(38) Zhmoidin, G. I.; Chatterjee, A. K. *Cem. Concr. Res.* **1985**, *15*, 442−452.

(39) Fischer, P.; Frey, G.; Koch, M.; Könnecke, M.; Pomjakushin, V.; Schefer, J.; Thut, R.; Schlumpf, N.; Bürge, R.; Greuter, U.; Bondt, S.; Berruyer, E. *Phys. B* **2000**, *276*, 146−147.

Table 1. Selected Data for Powder and Single-Crystal Mayenite Samples in $I\bar{4}3d$ Space Group[a]

param	C12A7-st	C12A7-eV	C12A7-esc	C12A7-osc
color	white-powder	green-powder	green-crysts	colorless-crysts
χ_0/emu·mol^{-1}	0.00033(1)	0.00311(1)	0.00300(1)	
R values[b]/%	1.62, 1.94	2.30, 2.93	3.70, 3.13	4.23, 4.20
a/Å	11.98681(1)	11.99215(1)	11.9904(3)	11.9824(5)
cages content	$\square_5O^{2-}$	$\square_{4.53}O_{0.53}{}^{2-}e_{0.94}{}^{-}$	$\square_{5-\delta}O_{1-\delta}{}^{2-}e_{2\delta}{}^{-}\ \delta \approx 0.5$	$\square_5O^{2-}$
Ca1(x 0 3/4)	$x = 0.8908(1)$	$x = 0.8910(1)$	$x = 0.8907(1)$	$x = 0.8905(1)$
Ca2(x 0 3/4)	$x = 0.9403(5)$	$x = 0.9500(5)$	$x = 0.9522(10)$	$x = 0.9311(6)$
Ca1/Ca2 ratio	0.857/0.143(2)	0.890/0.110(2)	0.910/0.090(6)	0.810/0.190(8)
Al1(x x x)	$x = 1.0184(1)$	$x = 1.0187(1)$	$x = 1.0188(1)$	$x = 1.0188(1)$
Al2(1 1/4 1/8)				
O1(x y z)	$x = 0.9002(1)$	$x = 0.9004(1)$	$x = 0.9008(2)$	$x = 0.9004(2)$
	$y = -0.1923(1)$	$y = -0.1918(1)$	$y = -0.1922(2)$	$y = -0.1925(2)$
	$z = 0.7132(1)$	$z = 0.7132(1)$	$z = 0.7132(2)$	$z = 0.7138(2)$
O2(x x x)	$x = 0.9356(1)$	$x = 0.9356(1)$	$x = 0.9353(2)$	$x = 0.9357(2)$
O3(x y z)	$x = 0.7228(7)$	$x = 0.6868(17)$	$x = 0.696(7)$	$x = 0.714(6)$
	$y = 0.1200(20)$	$y = 0.1146(21)$	$y = 0.109(7)$	$y = 0.093(7)$
	$z = -0.0016(28)$	$z = -0.0037(26)$	$z = 0.000(11)$	$z = -0.050(7)$
O3 occ factor	0.043(1)	0.022(1)	0.038(8)	0.037(10)
O3−Ca2/Å	2.182(18)	2.114(25)	1.99(9)	2.07(8)
	2.295(19)	2.349(25)	2.35(9)	2.81(8)
Ca1···Ca1/Å	5.615(2)	5.613(1)	5.619(2)	5.621(1)
Ca2···Ca2/Å	4.429(11)	4.197(13)	4.143(18)	4.648(10)

[a] The anisotropic temperature factors and the atomic positions for the absolute configuration are available in the CIFs files deposited at ICSD with numbers 416679, 416680, 416681, and 416682 for C12A7-st, C12A7-eV, C12A7-esc, and C12A7-osc, respectively. [b] R values for the powder diffraction studies are R_F for the NPD and SXRPD patterns, respectively. R values for the single-crystal studies are R_F for all reflections and for those with $F^2 > 2\sigma(F^2)$, respectively.

tion) and an X'Celerator detector. The samples were loaded in flat aluminum holders and scanned between 15 and 110° (2θ) in 0.03° steps on D5000 instrument and between 5 and 110° (2θ) in 0.004° steps on X'pert Pro diffractometer.

All powder diffraction data were analyzed by Rietveld refinement by using the GSAS suite of programs. Joint refinements of NPD and LXRPD (for C12A7-O_2 and C12A7-e samples) or SXRPD (for C12A7-st and C12A7-eV samples) data at RT were used to increase the number of observations, which yields better structural descriptions. The synthesis of C12A7-st was carried out to obtain 10 g for the joint NPD and SXRPD study. The preparation of this amount of sample led to a powder, which contained 2.23(3) wt % of $CaAl_2O_4$ as side phase. This impurity phase was taken into account in all Rietveld analyses. The C12A7 sample used to prepare C12A7-eV was single phase by laboratory powder diffraction. SXRPD data showed that C12A7-eV contained 1.18(2) wt % of $Ca_3Al_2O_6$ and 0.32(3) wt % of $CaAl_2O_4$ as impurity phases. These side phases were also taken into account in all Rietveld analyses.

Single-Crystal Diffraction. Crystallographic data for C12A7-esc/C12A7-osc were collected at room temperature on a Nonius CAD4 single-crystal diffractometer, using Mo Kα radiation (λ = 0.710 73 Å) and a graphite crystal monochromator. The unit-cell dimensions were determined from the least-squares fit of 25 reflections with θ between 25 and 30°. The intensity data of 3516/3868 reflections in hkl range (−16/19, −16/19, −16/19) to (16/19, 16/19, 16/19) and θ limits ($0° < \theta < 30/35°$) were measured using the $\omega-2\theta$ scan technique with a variable scan rate and a maximum scan time of 120 s/reflection. The intensity of the primary beam was checked throughout the data collection by monitoring 3 standard reflections every 60 min. A profile analysis was performed on all reflections;[40] μ(Mo Kα) = 2.292/2.297 mm^{-1}. Of the 422/629 unique reflections, 393/624 were observed with $I > 2\sigma(I)$. Lorentz−polarization corrections were applied, and the data were reduced to F_o^2 values. The positional parameters and the anisotropic thermal parameters of the all atoms were refined, with the exceptions of O3 and Ca2 sites, which were isotropically refined. The final cycle of full-matrix least-squares refinement based on 422/629 reflections and 30 parameters converged to a final value of R1($F^2 > 2\sigma(F^2)$) = 0.031/0.042 and wR2($F^2 > 2\sigma(F^2)$) = 0.079/0.118 using SHELXL-97 program.[41] Final difference Fourier maps showed no peaks higher than 0.72/2.14 e Å^{-3} nor deeper than −0.78/−1.04 e Å^{-3}. Both single crystals were investigated from RT to 110 K, showing no noticeable structural changes on cooling.

Results and Discussion

Synthesis and Basic Characterization. A new method to prepare mayenite electrides has been developed. This method, which uses a vanadium foil as oxygen drain, allows the use of powders. This is important because the chemical substitutions that permit tailoring some physical properties yield samples without congruent melting points, opening the possibility to prepare new powder doped-mayenite electrides.

Powder and single-crystal mayenites were initially characterized by absorption and magnetic measurements. Figure 1a shows the optical absorption spectra for C12A7-st and C12A7-eV. The main characteristic is the presence of a band at 2.75 eV in C12A7-eV, responsible for the green color, in full agreement with previous reports for medium electron-loaded samples.[8,19] Figure 1b shows the temperature dependence of the magnetic susceptibility for mayenite samples. White C12A7-st and C12A7-eox are mainly diamagnetic but green, both C12A7-eV and C12A7-esc develop noticeable Pauli paramagnetism (χ_0), ~3×10^{-3} emu/mol; see Table 1. The difference in χ_0 between green and white samples reflects the changes in the electronic density-of-states at the Fermi level due to the enhanced density of delocalized electrons. There is a secondary contribution to the susceptibility (Curie−Weiss, $C/T - \Theta$), in which C varies with

(40) Grant, D. F.; Gabe, E. J. *J. Appl. Crystallogr.* **1978**, *11*, 114−120.

(41) Sheldrick, G. M. *SHELXL-97. A computer program for refinement of crystal structures*; University of Gottingen: Gottingen, Germany, 1997.

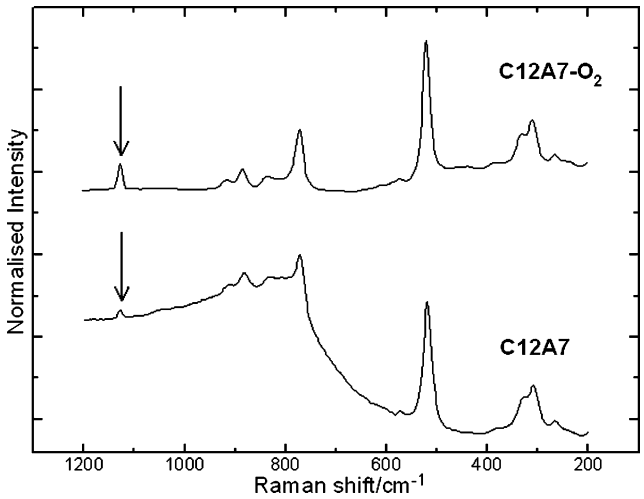

Figure 2. Raman spectra for C12A7-st and superoxide-loaded C12A7-O_2. The intensity enhancement of the band located at 1128 cm^{-1}, which is due to the superoxide anion vibration, is highlighted with arrows.

the sample and strongly depends on minor amounts of residual paramagnetic oxygen species into the cages, O_2^- for instance. The Weiss temperature (Θ) is very small and negative ($\Theta \sim -1$ K), as previously reported.[8]

Partial substitution of oxide anions by other oxygen species like superoxide anion, O_2^-, has been extensively studied/reported in recent years.[18,21,22,42] Figure 2 shows Raman spectra of C12A7-st and C12A7-O_2. The profiles are similar to those already reported.[21,42] The comparison of these spectra demonstrates the loading of a significant amount of superoxide anion, O_2^-. This is concluded because the intensity of the band located at 1128 cm^{-1}, which is assigned to the stretching mode in superoxide anion,[21,42,43] notably increases. In fact, higher amounts of superoxide anions can be inserted into the mayenite cages at intermediate temperatures and high oxygen pressures.[21,22]

Room-Temperature Crystal Structures. Crystal Structures of Oxymayenites. The accurate structural description of stoichiometric oxymayenite, $[Ca_{12}Al_{14}O_{32}]^{2+}\square_5O^{2-}$, is necessary because it is the parent member of several solid solutions which differ in the species clathrated into the cages: O_2^-;[16] OH^-;[15] H^-;[19] e^-.[8] The initial structural models used for the structural study of C12A7-st were those already reported,[13,14] which contain 6 atoms in the asymmetric part of the unit cell: Ca1, Al1, Al2, O1, O2, and "extraframework oxygen" O3. However, these structures did not fit adequately the powder diffraction data of C12A7-st. A disorder in the calcium location has been found and modeled through two close calcium positions (Ca1 and Ca2). The final refinement was carried out using anisotropic thermal displacement parameters for Ca1, Al1, Al2, O1, and O2, an isotropic thermal parameter for Ca2, and keeping the isotropic thermal parameter for O3 fixed to 0.03 $Å^2$ to avoid correlations with its occupation factor (occ f), which was varied. Diffraction patterns were very well reproduced as demonstrated by the low *R* factors shown in Table 1 and the excellent fit to the

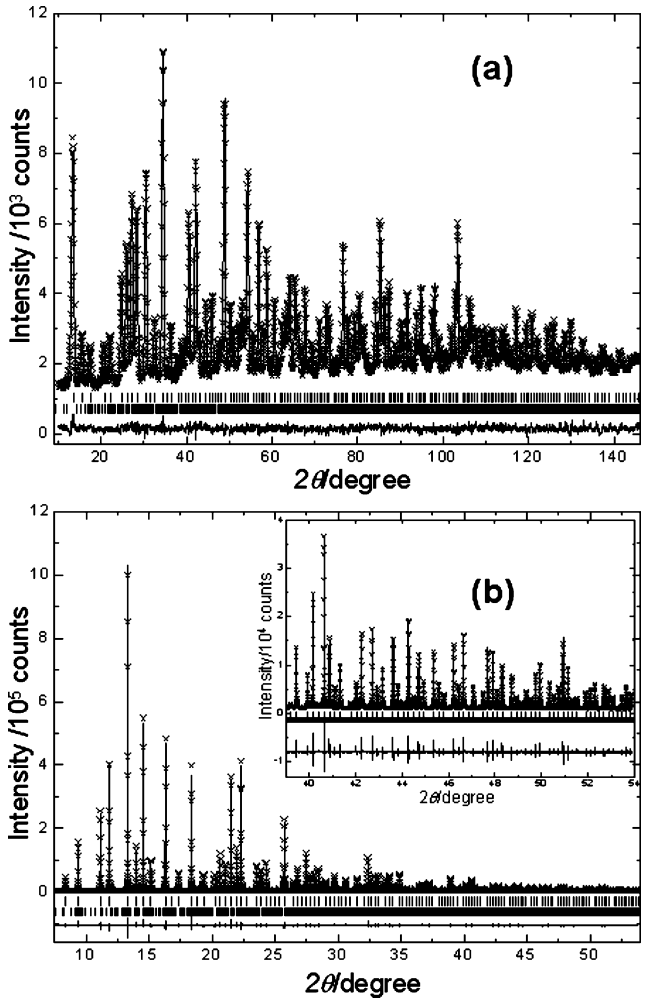

Figure 3. Observed (crosses), calculated (full line), and difference (bottom) RT powder diffraction patterns for C12A7-st: (a) neutron powder data ($\lambda = 1.154$ Å); (b) X-ray synchrotron powder data ($\lambda = 0.621$ Å). The inset shows an enlarged view of the high-angle region of the SXRPD pattern.

neutron and synchrotron data; see Figure 3. Data analysis showed that O3 is displaced out of the center of the cage and its refined occ f converged to 0.043(1). The resulting structural formula, $[Ca_{12}Al_{14}O_{32}]\square_5O_{1.03(2)}$, agrees very well with the nominal stoichiometry, $[Ca_{12}Al_{14}O_{32}]\square_5O$. The refined Ca1/Ca2 ratio was 0.857/0.143(2), which is not far from the expected fraction, 0.833/0.167 (=5/1), assuming that the disorder in calcium positions is due to the existence of empty and oxygen-filled cages as pointed out by theoretical calculations.[44]

The previously reported structural descriptions for oxymayenite[13,14] did not take into account the calcium disorder. This has now been corrected, and Figure 4a shows the framework of the mayenite structure and Figure 4b shows the two types of cages for C12A7-st. The Ca1···Ca1 distance in the empty cages is 5.62 Å; see Table 1. The Ca2···Ca2 distances strongly decrease to 4.43 Å in the oxygen-filled cages due to the attraction of the oxide anion, O3. The experimental value agrees very well with the theoretically

(42) Hayashi, K.; Matsuishi, S.; Ueda, N.; Hirano, M.; Hosono, H. *Chem. Mater.* **2003**, *15*, 1851−1854.
(43) Che, M.; Tench, A. *Adv. Catal.* **1983**, *32*, 1−148.
(44) Sushko, P. V.; Shluger, A. L.; Hayashi, K.; Hirano, M.; Hosono, H. *Phys. Rev. B* **2006**, *73*, 045120.

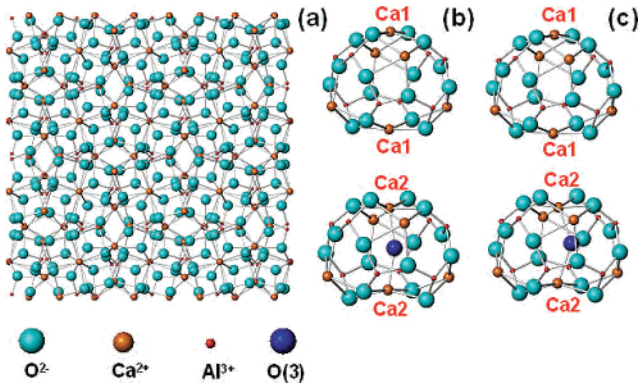

Figure 4. (a) Ball and stick view of the framework of mayenite $[Ca_{12}Al_{14}O_{32}]\square_5O$, where the loosely bound oxide anions, O3, are not shown for clarity. (b) Ball and stick view of the two type of cages in C12A7-st: (top) undistorted empty cage; (bottom) distorted filled cage. (c) Ball and stick view of the two type of cages in C12A7-eV: (top) undistorted empty cage; (bottom) very distorted filled cage.

predicted one, 4.42 Å, which was obtained by quantum mechanical calculations using an embedded cluster approach.[44] It must be noted that this work gave a Ca1···Ca1 distance of 5.54 Å for the empty cages. A very recent work by the same authors,[45] using B3LYP density functional, gave 5.64 Å, which agrees very well with our experimentally determined value, 5.62 Å; see Table 1.

The structural study for C12A7-O_2 was carried out through a joint Rietveld refinement of NPD and LXRPD data. The initial structural model was that previously described for stoichiometric oxymayenite, C12A7-st. However, this structural description was simplified by placing O3 atom at the special position in the center of the cage and using isotropic thermal displacement parameters for all atoms. This was carried out for the sake of comparison with the in-situ study (see below) where the statistic of the data was not very high. The usual parameters, histogram scale factors, background coefficients, zero-errors, peak shape coefficients, and unit cell edge, were varied. After convergence, the fits to the neutron and X-ray powder diffraction patterns were very good. It must be highlighted that the final refined occupation factor for O3 converged to 0.270(4), which is much higher than that corresponding to the stoichiometric compound (only oxide-loaded), 1/6 = 0.167. This is the expected behavior as the partial substitution of the loosely bounded oxide anions by anions such as O_2^- and O^- increases the amount of oxygen species into the cages. The disorder of calcium arises from the electrostatic interaction between the anions occluded in the cages and the calcium ions located in the poles of the S_4 symmetry axis of those filled cages.

Table 2 gives the atomic parameters for C12A7-O_2, and Table 3 reports the most important structural data. The amount of disordered calciums along the S_4 axis, Ca2, in C12A7-O_2 increases up to 0.274(8) because the higher amount of oxygen species into the cages, as expected. The intracage Ca····Ca distance in C12A7-O_2 is 5.652(6) Å for the empty cages, Ca1, and it on average decreases to 4.798(16) Å for cages occupied by oxygen species, Ca2. The

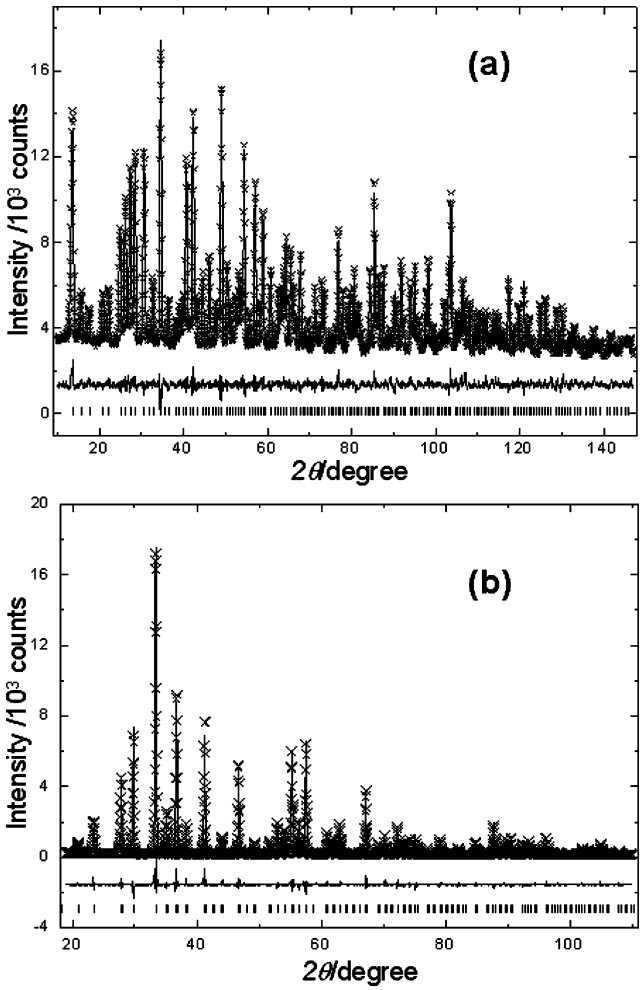

Figure 5. Observed (crosses), calculated (full line), and difference (bottom) RT powder diffraction patterns for C12A7-eV: (a) neutron powder data (λ = 1.154 Å); (b) X-ray synchrotron powder data (λ = 0.621 Å). The inset shows an enlarged view of the high-angle region of the SXRPD pattern.

corresponding values for stoichiometric C12A7-st are 5.615(2) and 4.429(11) Å, respectively; see Table 1. It is worth to note that the average Ca2···Ca2 distance in superoxide loaded mayenite is larger than that in stoichiometric mayenite because the superoxide anion is much more voluminous (and lower charged) than the oxide anion. Finally, it must be said that the structural model used for refining the crystal structure of C12A7-O_2 is approximate, as a single oxygen atom (at the center of the cages) has been used to describe the superoxide anions fraction.

Crystal Structures of Mayenite Electrides. The structural model used to fit the powder data for C12A7-eV was the same than that described above for C12A7-st. The quality of the fits was also very good as evidenced by the low R factors shown in Table 1 and the patterns displayed in Figure 5. A key structural difference between C12A7-eV and C12A7-st is the smaller O3 occ f, 0.022(1), as expected. The structural formula for C12A7-eV is $[Ca_{12}Al_{14}O_{32}]^{2+}\square_{4.53}O_{0.53(2)}{}^{2-}e_{0.94(4)}{}^-$, where the electron content was indirectly derived from the extraframework oxide concentration to balance the charges. The Ca1/Ca2 ratio was 0.890/0.110(2). It must be noticed that, with replacement of

(45) Sushko, P. V.; Shluger, A. L.; Hirano, M.; Hosono, H. *J. Am. Chem. Soc.*, in press. Published Online: Jan 4, 2007.

Table 2. Refined Atomic Parameters at Room Temperature for C12A7-O_2 from Joint Rietveld Refinement of Neutron and X-ray Laboratory Powder Diffraction Data

atom	Wyck posn	occ factor	*x*	*y*	*z*	U_{iso}/Å^2
Ca(1)	24d	0.726(8)	0.8892(2)	0	3/4	0.0073(3)
Ca(2)	24d	0.274(8)	0.9248(7)	0	3/4	0.0073
Al(1)	16c	1	1.01847(7)	0.01848(8)	1.01847(7)	0.0074(4)
Al(2)	12b	1	1	1/4	5/8	0.0059(4)
O(1)	48e	1	0.90028(8)	−0.19239(7)	0.71395(8)	0.0102(2)
O(2)	16c	1	0.93522(8)	−0.06478(8)	0.93522(8)	0.0106(3)
O(3)	12b	0.270(4)	1/8	0	3/4	0.03

Table 3. Selected Structural Data for C12A7-O_2 (white) and C12A7-e (green) Powder Samples

param	C12A7-O_2	C12A7-e
a/Å	11.982 15(9)	11.995 22(2)
O3 occ factor	0.270(4)	0.087(5)
Ca(2) occ factor	0.274(8)	0.092(5)
Ca(1)···Ca(1)/Å	5.652(6)	5.621(4)
Ca(2)···Ca(2)/Å	4.798(16)	4.39(4)
R values[a] (%)	2.28, 3.25	1.15, 2.05

[a] *R* values are R_F for the NPD and LXRPD patterns, respectively.

≈50% of the extraframework oxide anions by electrons, the unit cell volume expands by 0.045%.

The crystal structures of green C12A7-esc and colorless C12A7-osc have been studied by single-crystal diffraction. The data analyses corroborate all main findings of the powder diffraction studies; see Table 1. The unit cell of the electride is larger than that of the stoichiometric oxide. The Ca1/Ca2 ratio for C12A7-osc was 0.810/0.190(8), which is also not far from the expected value, 5/1. This fraction changes to 0.910/0.090(6) for C12A7-esc. Unfortunately, the high errors in the O3 occ f, Table 1, do not allow extracting the electron concentration in C12A7-esc from X-ray single-crystal diffraction.

The first structural description of mayenite electride is reported, Table 1, and two key findings are obtained. First, the overall electron concentration of C12A7-eV, $[Ca_{12}Al_{14}O_{32}]^{2+}\square_{4.53}O_{0.53}{}^{2-}e_{0.94}{}^{-}$, was indirectly determined from the loosely bounded O3, by using NPD. Taking into account the errors in the neutron diffraction analysis ($\pm 3\sigma$), the electron concentration for this sample is in the range $(0.9-1.3) \times 10^{21}$ cm^{-3}, which includes both localized and delocalized electrons. Second, it is the indirect evidence of, at least partial, electron trapping into the cages. The Ca2••·Ca2 distances drops from 4.43 Å in C12A7-st (and C12A7-osc) to 4.20 Å in C12A7-eV (and C12A7-esc); see Figure 4c and Table 1. The origin of this (extra)-distortion is still not clear, and it deserves further theoretical and experimental work. These average extra displacements may reflect a polaronic effect, i.e., the stabilization of the electron due to the lattice relaxation. However, a very recent theoretical study in this type of materials[45] concludes that the Ca2···Ca2 distances in electron-filled cages are larger than 5.05 Å. Hence, the big Ca2···Ca2 distortion observed in C12A7-eV may be likely due to the remaining oxide anions inside the cages, which are moved away from each other. It must be emphasized that for partially electron loaded electrides, $[Ca_{12}Al_{14}O_{32}]^{2+}\square_{5-\delta}O_{1-\delta}{}^{2-}e_{2\delta}{}^{-}$ ($0 < \delta < 1$), there are three types of cages: empty; filled with oxide anions; filled with localized electrons, still, in unknown position(s). Unfortunately, all refinements with three types of Ca atoms were unstable due to the relatively low concentration of distorted cages.

Variable-Temperature Studies. Electride at High Temperature. A selected region of the SXRPD thermodiffractometries for C12A7-st and C12A7-eV is given in Figure 6. The diffraction peaks for C12A7-eV are not split with temperature; conversely, those for C12A7-st are broader and display clear shoulders between 573 and 773 K. This split has been modeled by introducing a second mayenite phase with smaller unit cell (C12A7-st_2nd). The unit cell volumes resulting from the analysis of all diffraction data are given in Figure 7. The linear fits of the volumes with temperature, 300−873 K range, are also displayed. The calculated volumetric thermal expansion coefficients were $13.2(1) \times 10^{-6}$, $14.6(1) \times 10^{-6}$, and $15.4(1) \times 10^{-6}$ K^{-1}, for C12A7-eV, C12A7-st, and C12A7-st_2nd, respectively. It must be noticed that the thermal expansion coefficient for the electride is smaller than that of the oxymayenite. Furthermore, this very high resolution SXRPD thermal study shows that the electride is single phase in all explored temperature range.

In-Situ Electride Formation Study. The formation of the electride can be followed in-situ by NPD. To do so, the oxymayenite was tightly pressed in the vanadium can and heated under vacuum. Figure 8 displays the evolution of the loosely bounded oxygen occupation factor, O3, on heating. Between RT and 500 K, the O3 occupation factor remained nearly constant at 0.27. A small drop to 0.24 was observed at 573 K, and then, this value remained constant up to 973 K. Above 1000 K, an important decrease of the O3 occupation factor was observed. The refined value dropped well below 0.167, which is the oxygen content for stoichiometric mayenite. Occupation factors below that critical number indicate that the electride is being formed. The oxygen species are partially removed from the cages and react with the vanadium can. The minimum refined occupation factor for O3 was 0.05(1), which was obtained at the highest temperature, 1373 K. Figure 8 also shows the evolution of cell volume of the mayenite sample with temperature.

We propose the following mechanism for the electride formation under these conditions: (i) First, there is migration of oxide anions (or other oxygen species occupying the cages) from the bulk grains to the vanadium container walls (this migration is activated at high temperatures). (ii) Then, there is oxidation reaction at the metal surface to produce vanadium oxide. [Unfortunately, the oxide layer in the metal

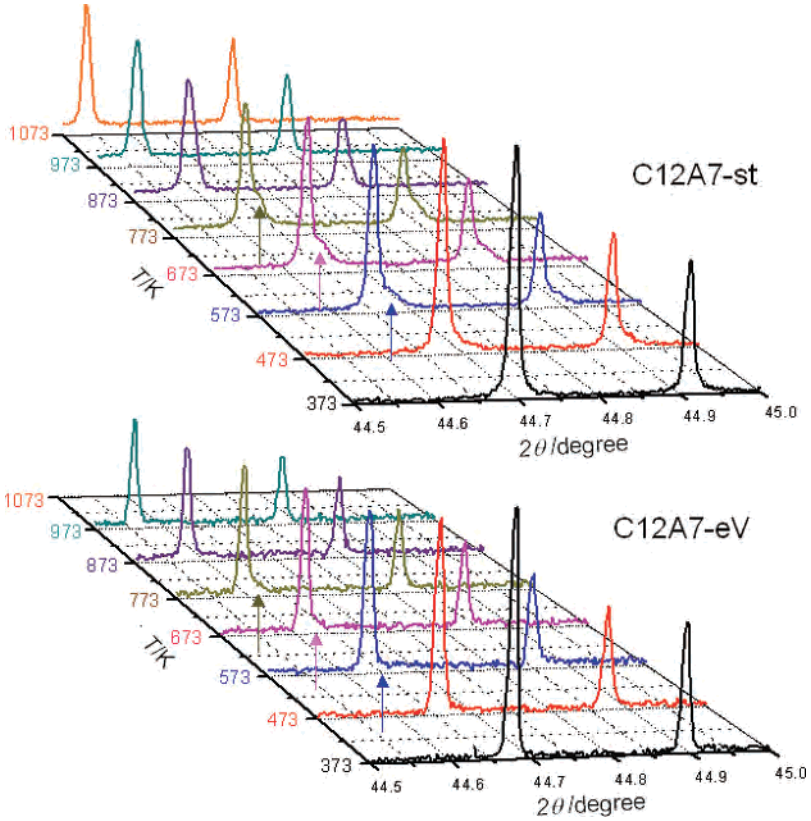

Figure 6. Selected region of the SXRPD thermodiffractometries for C12A7-st and C12A7-eV. The arrows highlight the presence of a second segregated phase (C12A7-st_2nd) at intermediate temperature for C12A7-st but not for C12A7-eV.

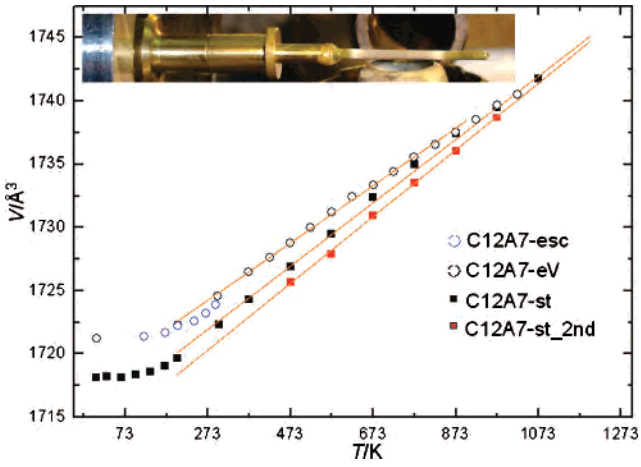

Figure 7. Temperature variation of the unit cells for mayenite samples. The values for C12A7-st (solid squares) and C12A7-eV (black open circles) were derived from SXRPD and NPD. The data for C12A7-esc (blue open circles) were determined from single-crystal diffraction. The values for the two high-temperature phases in C12A7-st are given as solid squares (black and red). The top inset shows the capillary containing the C12A7-eV powder after the high-temperature experiment evidencing the oxidation of the electride (grayish-white at the center and green at the extremes). The oxidation took place likely above 773 K as deduced from the curvature toward smaller unit cell volumes.

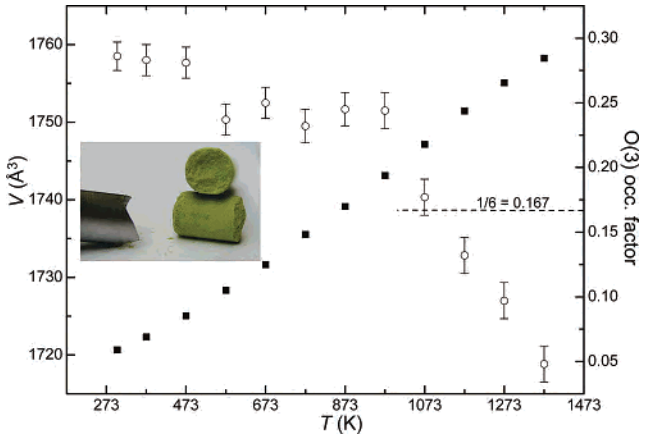

Figure 8. C12A7-O_2 cell volume (solid squares, left axis) and O3 occupation factor (open circles, right axis) versus temperature on heating along the in-situ NPD experiment. The photograph in the inset shows the final mayenite sample (note the green color) and the brittle broken vanadium can at the end of the experiment.

is too thin (and/or amorphous) and it was not observed in the NPD patterns. However, the vanadium container becomes brittle after the experiment (see photograph inset in Figure 8), which is an indirect proof of the container partial oxidation]. (iii) The electrochemical reaction at the ceramic−metal interlayer boundary yields free electrons which migrate through the porous framework to counterbalance the charges. This process renders a green-colored electride, as can be seen in the inset of Figure 8.

In-Situ Electride Decomposition Study. Side phases appeared during the kinetic study at the final temperature, 1373 K. They were first identified, and latter quantified in the refinements, using the previously published structural models: $Ca_5Al_6O_{14}$ (C5A3);[46] and $Ca_3Al_2O_6$ (C3A).[47] The

(46) Vincent, M. G.; Jeffery, J. W. *Acta Crystallogr., Sect. B: Struct. Sci.* **1978**, *34*, 1422−1428.
(47) Mondal, P.; Jeffery, J. W. *Acta Crystallogr., Sect. B: Struct. Sci.* **1975**, *31*, 689.

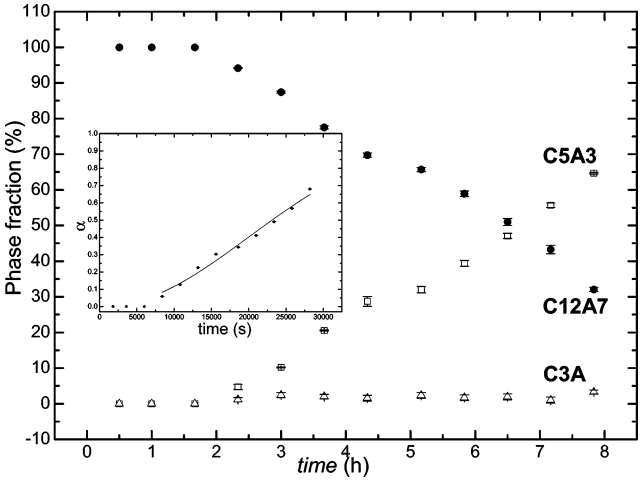

Figure 9. Variation of phase fractions versus time at 1373 K for C12A7 (solid circles), C5A3 (open squares), and C3A (open triangles). The inset shows the conversion of C12A7 with time fitted to the Avrami equation in the $0.05 \leq \alpha \leq 0.7$ region.

unit cell volume of C12A7 and the O3 occupation factor did not significantly change along the kinetic experiment at 1373 K. However, it must be noted that the mayenite framework is not stable at high temperature (under reducing conditions) in the absence of template anions, such as O^{2-}, O_2^-, OH^-, or halides. It has been reported that melts with stoichiometries near to that of C12A7 crystallize in the mayenite structure only when there are some template species allowing for the nucleation of the mayenite open framework. In the absence of template anions, this nucleation cannot occur and the melt crystallizes in a C5A3 and C3A mixture from temperatures below 1773 K[48] and in a CA ($CaAl_2O_4$) and C3A mixture when crystallized from a melt at temperatures above 1873 K.[25b,48] Our NPD data clearly indicate that the mayenite structure is unstable at 1373 K under reducing conditions. C12A7 seems to decompose according to the following reaction:

$$4Ca_{12}Al_{14}O_{33} \rightarrow Ca_5Al_6O_{14} + Ca_3Al_2O_6 \qquad (1)$$

Figure 9 shows the phase evolution at 1373 K under strong dry-reducing conditions. C12A7 decomposes to give C5A3 and C3A as the unique observed crystalline phases. The decomposition reaction has been quantitatively confirmed from the phase analysis of the room-temperature powder patterns of the final sample, C12A7-e. The Rietveld refinement gave the following phase assemblage: 22.4(2)% of C12A7; 71.7(1)% of C5A3; 5.67(2)% of C3A. The decomposition of 77.6 g of C12A7 would yield, according to the stoichiometry of reaction 1, 73.8 g of C5A3 and 3.8 g of C3A. There is a relatively good agreement between both set of values, and thus, the stoichiometry of the thermal decomposition reaction has been verified.

The kinetic behavior of mayenite decomposition was investigated by inspecting the relationship between the transformed fraction (α) and reaction time (t). A nuclei-growth kinetic equation may be empirically expressed in a simplified form (Avrami−Erofe'ev equation) as

$$1 - a = \exp[-(kt)^n] \qquad (2)$$

where k is the apparent rate constant and the exponent, n, often referred to as the "Avrami exponent", depends on the mechanism and geometry of nucleation and growth, $n = \beta + \lambda$, where β is the number of steps involved in nucleus formation and λ is the number of dimensions in which the nuclei grow.[49−51] Limiting values of n connected with sound mechanisms of nuclei-growth processes lie between 0.5 and 4. For instance, an instantaneous nucleation with the two-dimensional linear growth gives rise to $n = 2$. An instantaneous nucleation with three-dimensional linear growth gives rise to $n = 3$. Conversely, if the limiting step is the nucleation and the growth is fast enough, the obtained values for n may be 1.0 or smaller.

The kinetic data presented in Figure 9 have been fitted to eq 2. Two fits have been carried out including the induction period (approximately 90 min) and second using the data $0.05 \leq \alpha \leq 0.7$. The result for this second fit is shown in the inset of Figure 9, and it gave $n = 2.06(13)$ and $k = 4.1(1) \times 10^{-5}$ s^{-1}. The fit including the induction period gave $n = 2.11(15)$. Thus, from the Avrami exponent, it can be said that the mayenite isothermal decomposition, at 1373 K, is limited by a layer growth around the mayenite particles and nucleation is not limiting the reaction rate.

Finally, a C12A7-e sample was studied by joint Rietveld refinement of NPD and LXRPD data. In addition to the quantitative phase analysis of the mixture, the crystal structure of the resulting green mayenite was analyzed. The final Rietveld plots are given as Supporting Information. The key structural data are given in Tables 2 and 3. The refined O3 occupation factor "ex-situ" was 0.083(4), which is much lower than that of the stoichiometric material, $1/6 = 0.167$, indicating that an electride has been formed. This value justifies the green color of the final sample as it only contains $Ca^{2+}-Al^{3+}-O^{2-}-e^-$. Another (indirect) evidence of the electride formation is the unit cell variation; see Table 3, which increases with the electron-loading, as described above for C12A7-eV. The Ca2···Ca2 distance along the S_4 axis also decreases from 4.798(16) Å in C12A7-O_2 to 4.33(4) Å in C12A7-e.

Conclusions

Accurate structural data for white oxymayenite, $[Ca_{12}Al_{14}O_{32}]\square_5O$, and green electride, $[Ca_{12}Al_{14}O_{32}]^{2+}\square_{4.53}O_{0.53}{}^{2-}e_{0.94}{}^-$, are reported from joint Rietveld refinements of neutron and synchrotron X-ray powder diffraction data and also from single-crystal diffraction. Neutron powder diffraction has also been used to follow in-situ the mayenite-electride formation. The superoxide-loaded sample has been heated under vacuum in a vanadium can, and a fraction of the loosely bounded oxygen species has been removed

(48) Zhmoidin, G. I.; Chatterjee, A. K. *Cem. Concr. Res.* **1984**, *14*, 386−396.

(49) (a) Avrami, M. *J. Chem. Phys.* **1939**, *7*, 1103. (b) Avrami, M. *J. Chem. Phys.* **1940**, *8*, 212. (c) Avrami, M. *J. Chem. Phys.* **1941**, *9*, 177.

(50) Erofe'ev, B. V. *C. R. Dokl. Akad. Sci. URSS* **1946**, *52*, 511.

(51) Brown, W. E.; Dollimore, D.; Galwey, A. K. *Chemical Kinetics, Vol. 22, Reactions in the Solid State*; Elsevier: Amsterdam, 1980.

leaving electrons into the mayenite cages. Under the investigated experimental conditions, the reducing reaction takes place incompletely between 1073 and 1373 K. Furthermore, mayenite subjected to prolonged heating at 1373 K (under high vacuum) decompose to give C5A3 and C3A instead to yield a mayenite with higher amount of free electrons in it. The kinetics of this isothermal decomposition reaction has been analyzed by the Avrami−Erofe'ev equation, and the obtained exponent ($n = 2$) is compatible with an instantaneous nucleation and a two-dimensional linear growth of the new phases.

Acknowledgment. This work was partially performed at the SINQ (Paul Scherrer Institut, Villigen, Switzerland) and at the ESRF (Grenoble, France). We thank Dr. Brunelli (ESRF) for helping during the synchrotron experiment. Dr. Beran (CSIC) is thanked for recording the magnetic data. Financial support from MAT2003-7483-C02 and MAT2006-11080-C02 research grants is gratefully acknowledged.

Supporting Information Available: Neutron and synchrotron X-ray RT powder diffraction pattern fits for C12A7-O_2 and C12A7-e samples. This material is available free of charge via the Internet at http://pubs.acs.org.

IC0700497